Available online at www.keaipublishing.com/en/journals/journal-of-magnesium-and-alloys/

ScienceDirect

Journal of Magnesium and Alloys 13 (2025) 1099–1115

www.elsevier.com/locate/jma

Full Length Article

Unusual twin induced recrystallization and corresponding texture optimization in a cold rolled Mg-Gd-Zr alloy during annealing

Ning Lv[a,b], Lingyu Zhao[c,*], Hong Yan[a,d], Boyu Liu[e], Rongshi Chen[a,*], Zhiwei Shan[e]

[a] *Shi-changxu Innovation Center for Advanced Materials, Institute of Metal Research, Chinese Academy of Sciences, 72 Wenhua Road, Shenyang 110016, China*

[b] *School of Materials Science and Engineering, University of Science and Technology of China, 72 Wenhua Road, Shenyang 110016, China*

[c] *School of Materials Science and Engineering, Shenyang Ligong University, Shenyang, 110159, China*

[d] *School of Materials Science and Engineering, Shandong University of Science and Technology, Qingdao, Shandong 266590, China*

[e] *Center for Advancing Materials Performance From the Nanoscale (CAMP-Nano) & Hysitron Applied Research Center in China (HARCC), State Key Laboratory for Mechanical Behavior of Materials, Xi'an Jiaotong University, Xi'an 710049, China*

Received 6 February 2024; received in revised form 21 March 2024; accepted 15 April 2024
Available online 7 May 2024

Abstract

Twins play an important role in the texture transition during annealing. In a cold rolled high rare earth content magnesium (Mg) alloys with {10–12} extension twins, {11–21} extension twins, {10–11} compression twins and {10–11}-{10–12} double twins and frequent twin-twin interactions, quasi-in-situ electron backscatter diffraction method was used to observe the twin induced static recrystallization (SRX) and related effect on texture during annealing. The results show that basal component was consumed owing to the SRX occurred in basal oriented {10–12} twins and SRXed grains with several specific orientations show preferential grain growth. SRX widely operated in the {10–12} extension and {11–21} extension twins, but absent in most {10–11} compression and {10–11}-{10–12} double twins, which is different to traditional twin induced SRX. Most compression/double twins detwinned while only partial tension twins detwinned. Operation of {11–21} twins and resultant twin-twin interaction facilitate the formation of serrated twin boundaries, which can serve as nucleation sites. Activation of <c + a> dislocation and related dislocation interaction in high dislocation density areas promote the formation of new grain boundaries and related SRX. Profuse <c + a> dislocations in basal oriented twins release the strain accumulation in compression/double twins and thus result in the absence of SRX. The twin size difference, storage energy and dislocation-twin interaction commonly functioned to the detwinning during annealing. The near-coincide site lattice boundaries that show high mobility were considered to be the important contributor to the preferential grain growth of SRXed grains.

Keywords: Magnesium alloy; {11–21} twin; Texture; Static recrystallization; Detwinning.

1. Introduction

In magnesium (Mg) alloys, texture significantly influence the mechanical property [1–5]. Usually, there will always be a basal texture formed during rolling or extrusion, which greatly restrict the mechanical property improvement and the wider application of Mg alloys [6–8]. Over the past decades, many efforts had been taken on the weakening of basal texture and activating twinning had attracted extension attention owing to the significant reorientation of parent grain after twinning operate [9–11]. For example, by designing specific strain path change tests, the basal texture in the wrought Mg alloy can be fixed through {10–12} twinning behaviors and corresponding interaction of {10–12} twin variants [9,10]. Further, the {10–12} twinning behaviors will also obstruct the formation of basal texture when special texture, i.e., the rare earth (RE) texture, exist in the billet during deformation progress [11]. Activating {10–12} twin variants through multi-directional impact

* Corresponding authors.
E-mail addresses: lyzhao202207@163.com (L. Zhao), rschen@imr.ac.cn (R. Chen).

https://doi.org/10.1016/j.jma.2024.04.015

forging had also been used to prepare the weak textured high performance Mg alloys [12,13].

In addition, twins can also optimize texture through twin-induced recrystallization [12,14-16]. In Mg alloys, different twins show various static recrystallization (SRX) behaviors. It is widely observed that compression twin and double twin will always act as nucleation sites and recrystallize at the very beginning during annealing [14,17,18]. The new grains that formed within compression/double twins usually show various orientation and thus weaken the basal component [19,20]. However, these compression/double twins induced SRXed grains can hardly grow into parent grains, which restricted their contribution to texture randomization [18]. In Mg alloys with twin-twin impingements, it is proposed that the grains which nucleate at the intersection of double twins and the impingements of double twins and grain boundaries can grow up and consume the adjacent deformed microstructure, which exhibit excellent contribution on basal texture weakening [14,21]. Different from the conditions in compression twin and double twin, SRX rarely occur within {10–12} tension twin in cold rolled Mg alloy but operate in the {10–12} twins in the forged Mg alloys, and such a difference has been illustrated as the high storage energy within {10–12} twins in the forged alloy [14,22]. Considering the above statements, the nature of twin induced SRX seems still controversial.

Recently, by analyzing the SRX in Mg-Zn-Gd alloy, it has been proposed that the nucleation and growth of SRXed grains as well as related effects on texture were significantly influenced by the type of dislocation, solute atom segregation, coincident site lattice (CSL) grain boundaries and so on [23–25]. Nevertheless, the above microstructure characteristics has rarely been considered in the research on twin induced SRX. Additionally, {11–21} twinning can activate when RE content large than ∼7 (wt.%) and will become more active with the RE content increasing [26–29]. {11–21} twinning has received extensive attention [26,30] in recent years but their contribution on SRX is still confusing.

To settle the above issues, we tracked the twin induced SRX and grain growth progress during annealing through a quasi-in-situ electron backscatter diffraction (EBSD) method in this work. A cold rolled Mg-17.5Gd-Zr (wt.%) with various twinning behaviors (including {10–12}, {11–21}, {10–11} and {10–11}-{10–12} double twins) and twin-twin interaction was used for annealing test to observe the texture and microstructure evolution. Systematic analyses were carried out to approach the nature of twin induced SRX and subsequent grain growth. This work will offer an insight on texture controlling through twin induced SRX and better facilitate the fabrication of high RE content Mg alloys with excellent performance.

2. Experiments and methods

The material used in this study was a cold rolled Mg-17.5Gd-Zr (wt.%) alloy. Before extrusion, the chemical compositions of cast ingot were determined by using inductively coupled plasma atomic emission spectroscopy. The Gd content was ∼17.5(wt.%), while the Zr content was < 0.1 (wt.%). Extruded plate with dimension of ∼100 mm (ED) × 12 mm (ND) × 50 mm (TD) was used for cold rolling (ED, ND and TD represent the extrusion direction, normal direction and transverse direction of the extruded plate, respectively) and there is <0001> fiber texture in the extruded plate. The plate was cold rolled along ED with accumulated reduction of ∼19% in 4 passes and reduction for per pass was ∼5%.

The as-extruded and cold rolled samples used for EBSD observation was firstly mechanical polished and then ion etched using Leica RES102. Quasi-in-situ EBSD scans of the cold rolled sample were taken after annealing at 440 °C for 2 min, 5 min, 10 min, 15 min, 25 min and ion etchings were carried out on the sample before each scan to remove the oxide layers that formed during annealing. The material that used for optical microcopy (OM) was mechanical polished and then etched using alcohol solution containing 4% of nitric acid (volume fraction). For transmission electron microscopy (TEM) observation, 3 mm-diameter discs with thickness of ∼30 μm were punched from the foil specimens and then argon-ion polished on GATAN 695. After TEM observation, EBSD was carried out on the TEM sample to identify the twin boundary. EBSD scans were conducted on FEI Quattro S SEM and Zeiss Gemini 360 SEM equipped with EDAX-TSL EBSD system. JEOL JEM-2100F equipped with energy-dispersive X-ray spectroscopy (EDX) was used to finished TEM observation. The data processing progress is same to our previous work [31].

3. Results

3.1. Microstructure of the as-extruded and cold rolled samples

The EBSD results of the as-extruded sample are show in Fig. 1 and microstructure with fully recrystallized grains can be observed (Fig. 1a). The extruded alloy shows ⟨0001⟩ fiber texture (Fig. 1b and c) and such a texture usually occurred in extruded high Gd content Mg alloys [32,33]. Obviously, ⟨0001⟩ fiber texture is favorable for activating {10–12} and {11–21} extension twinning behaviors when loaded perpendicular to ND [31]. Therefore, cold rolling was conducted on the as-extruded alloy to activate twinning behaviors.

The microstructure of the cold rolled sample is displayed in Fig. 2 and twins with various morphology can be observed. Frequent twin-twin intersection can be observed (Fig. 2a) and even the twins with small size show curved morphology (Fig. 2b and c), which can be attribute to the twin-twin and dislocation-twin interaction [31]. Further, secondary phase can be rarely seen due to the high extrusion temperature (470 °C) and low rolling temperature (room temperature), which indicate that the particle stimulated nucleation could rarely operate during annealing.

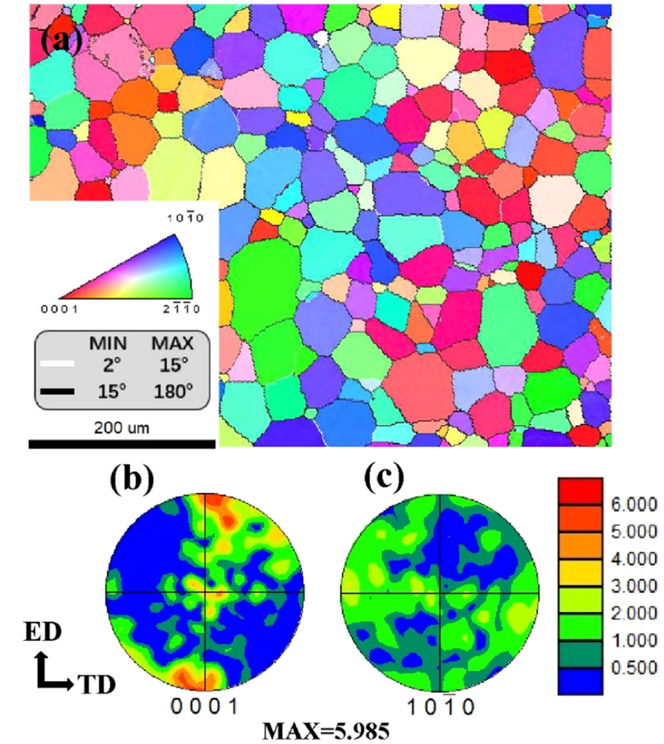

Fig. 1. EBSD results of the as-extruded sample. (a) Inverse pole figure map, (b) (0001) and (c) (10–10) pole figures.

3.2. Microstructure and texture evolution of the cold rolled samples during annealing

Fig. 3 shows the microstructure evolution of the cold rolled sample during annealing. Different twin boundaries, random high angle grain boundaries (HAGBs) were marked as different colors. The angle deviation used to identify twin boundaries was within 5°. From the grain boundary maps (Fig. 3g-l), various twinning behaviors and related twin-twin intersection can be identified. {11–21} twins and {10–11}-{10–12} double twins always occurred in the twinned grains with {10–12} twins. Besides, it has been confirmed that large amount of random HAGBs and irregular morphology of twin boundaries are induced by the dislocation-twin and twin-twin interaction [31]. The misorientation angle distribution of quasi-in-situ EBSD observation was summarized in Fig. 4. As shown in Fig. 4a and b, four peaks around 0–10°, 30–40°, 50–60° and 80–90° can be identified. The axis and angle distribution of the cold rolled sample (Fig. 4b) indicate that the four peaks represent the low angle grain boundaries (LAGBs), {11–21} extension twin boundaries and {10–11}-{10–12} double twin boundaries (30–40°), {10–11} compression twin boundaries and {10–12} twin variant intersection (50–60°) and {10–12} twin boundaries. During annealing, there were apparent decreasing of LAGBs and {10–12} twin boundaries, while other peaks hardly changed, which may in-

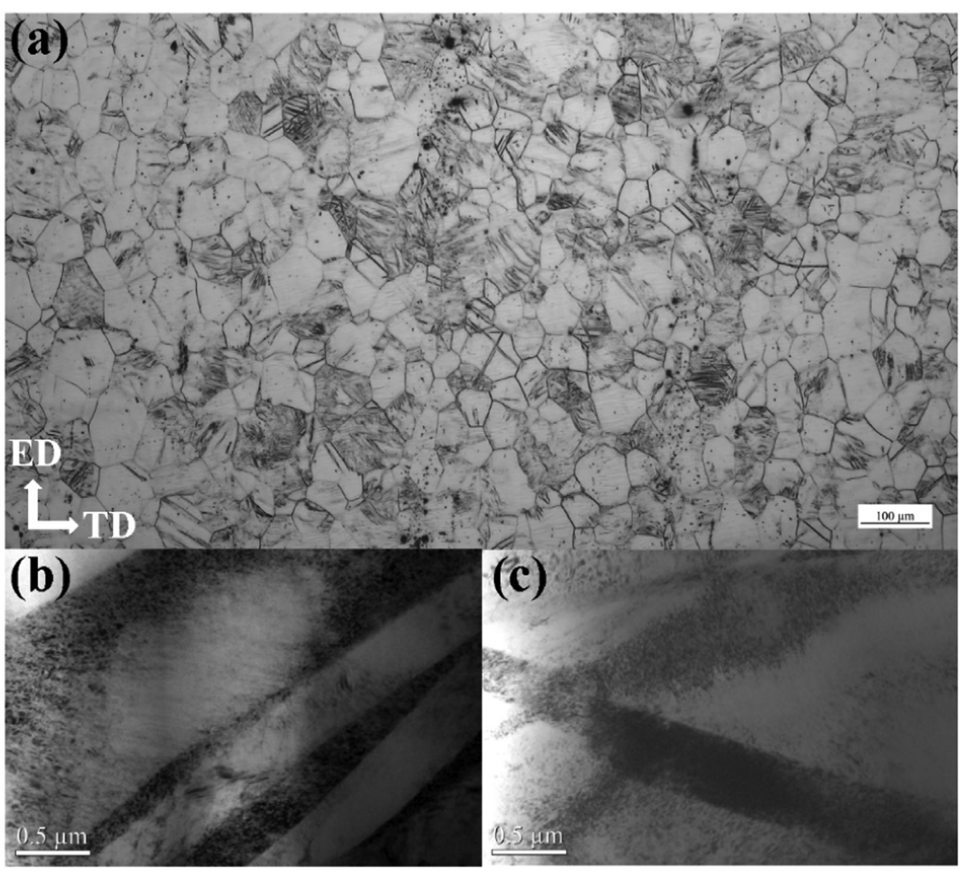

Fig. 2. Microstructure of the cold rolled sample. (a) OM image and (b, c) TEM image of twins.

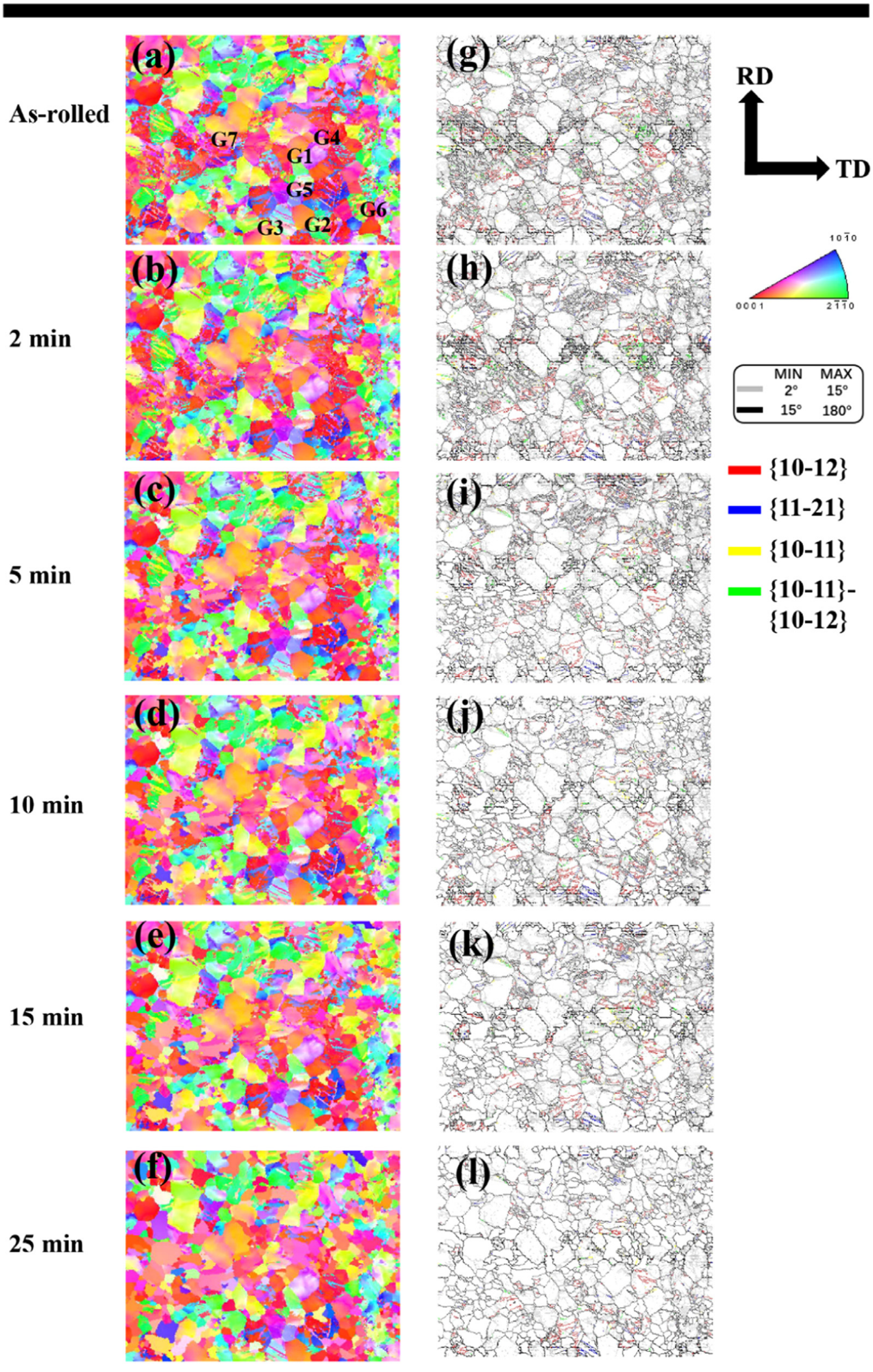

Fig. 3. Quasi-in-situ EBSD results of the microstructure. (a-f) inverse pole figure maps and (g-l) corresponding grain boundary maps during annealing with various time: (a, g) cold rolled samples, (b, h) 2 min, (c, i) 5 min, (d, j) 10 min, (e, k) 15 min and (f, l) 25 min.

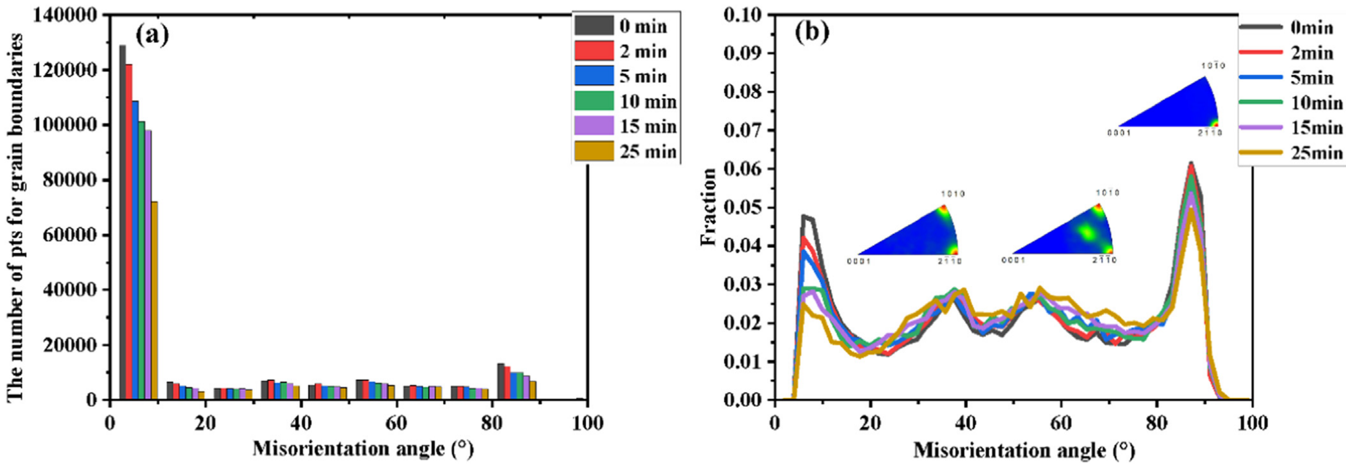

Fig. 4. Misorientation distribution evolution during annealing: (a) the number of pts for grain boundaries and (b) the fraction of grain boundaries between identified grains.

dicate the better thermal stability of other twin boundaries. The stability of twins will be discussed in Section 4.

Fig. 5 shows the KAM and grain size distribution evolution of quasi-in-situ EBSD results. As displayed in Fig. 5a-f, the KAM value gradually decreased with the annealing time increasing. In addition, as shown in Fig. 5g-i, the grain size distribution and average grain size hardly changed during the first 5 min, which can be inferred that SRX operated and no obvious grain growth occurred. With the annealing time increasing (5–25 min), the aera fraction of the small-sized grains decreased and the grain size distribution tend to approach the distribution of fully recrystallized as-extruded alloy, which indicate that the grain growth of the SRXed grains facilitate the strain accumulation decreasing greatly at this stage. (0001) pole figures of the quasi-in-situ EBSD results were depicted in Fig. 6a-f. A basal component and two non-basal components can be observed. During annealing, the basal component became weakened constantly while one of the non-basal components steady strengthened. As concluded from Fig. S1, the basal component was mainly result from the basal oriented {10–12} twins. Considering the decline of {10–12} twin boundaries (Fig. 4b), the basal component weakening can be mainly attributed to the consumption of basal oriented {10–12} twins. The pole figures evolution of SRXed grains are extracted and shown in Fig. S2. It can be observed that several non-basal oriented poles strengthened gradually during annealing, which indicate the preferential grain growth of the SRXed grains and the details will be discussed in Section 4.3.

3.3. Evolution of twin and recrystallization during annealing

In this section, several typical grains were picked out to analyze the thermal stability and twin induced SRX. Twin boundaries, LAGB and HAGB are highlighted by different colors. For the convenience of understanding, the fonts which mark twins in the scattered pole figures were highlighted as the same color to corresponding twin boundaries. In addition, for better observing the microstructure of twinned grains, the enlarged inverse pole figures of G4, G5 and G7 are displayed in Fig. S4.

Twinned grains with {11–21} and {10–12} twins (G3 and G4) are shown in Fig. 7 and SRX rarely occurred during annealing. One basal oriented {10–12} twin variant T1 and one {11–21} variant T2 activated in G3 (Fig. 7a) and most {11–21} twin crystals remained constant during annealing. As shown in black circles in Fig.7a, partial {11–21} twin crystal expanded while the {10–12} twin crystal shrunk consecutively during annealing. Several {10–12} twin crystals and partial parent grains (marked by black arrows in cold rolled G3) with small size eliminated during annealing. One SRXed grain formed after 10 min annealing and this grain finally consumed by adjacent twin crystals after 25 min annealing. In G4, basal oriented {10–12} twin dominated the twinning behaviors and only one {10–12} twin variant (T1) activated. One {11–21} twin variant (T2) with narrow shape activated. As highlighted by green and yellow arrows (Fig. 7b), one {10–11} twin variant and several {10–11}-{10–12} twin variants activated within T1. T2, {10–11} twin and most {10–11}-{10–12} twins eliminated after annealing for 25 min. Partial parent grains were also consumed by {10–12} twins, too. In addition, although the boundaries of twinned grains (including twin-free grains in Fig. S3) show serrated morphology, SRX can be rarely seen in these grains without complex twin-twin interaction.

The typical twinned grains with SRX are shown in Figs. 8 and 9. G5 shows the grain with complex twin-twin interaction and basal oriented {10–12} twinning dominate the twinning behaviors. One {10–12} (T1) and three {11–21} twin variants (T2-T4) activated, and various {10–11}-{10–12} double twin variants and one {10–11} compression twins activated within {10–12} twins (Fig. 8a). Similar to the orientation of twins in G4 (Fig. 7b), the {10–12} twin variant shows basal orientation while other twin crystals show non-basal orientation. During annealing, most compression twins and double twins eliminated. After 2 min annealing (Fig. 8b and f),

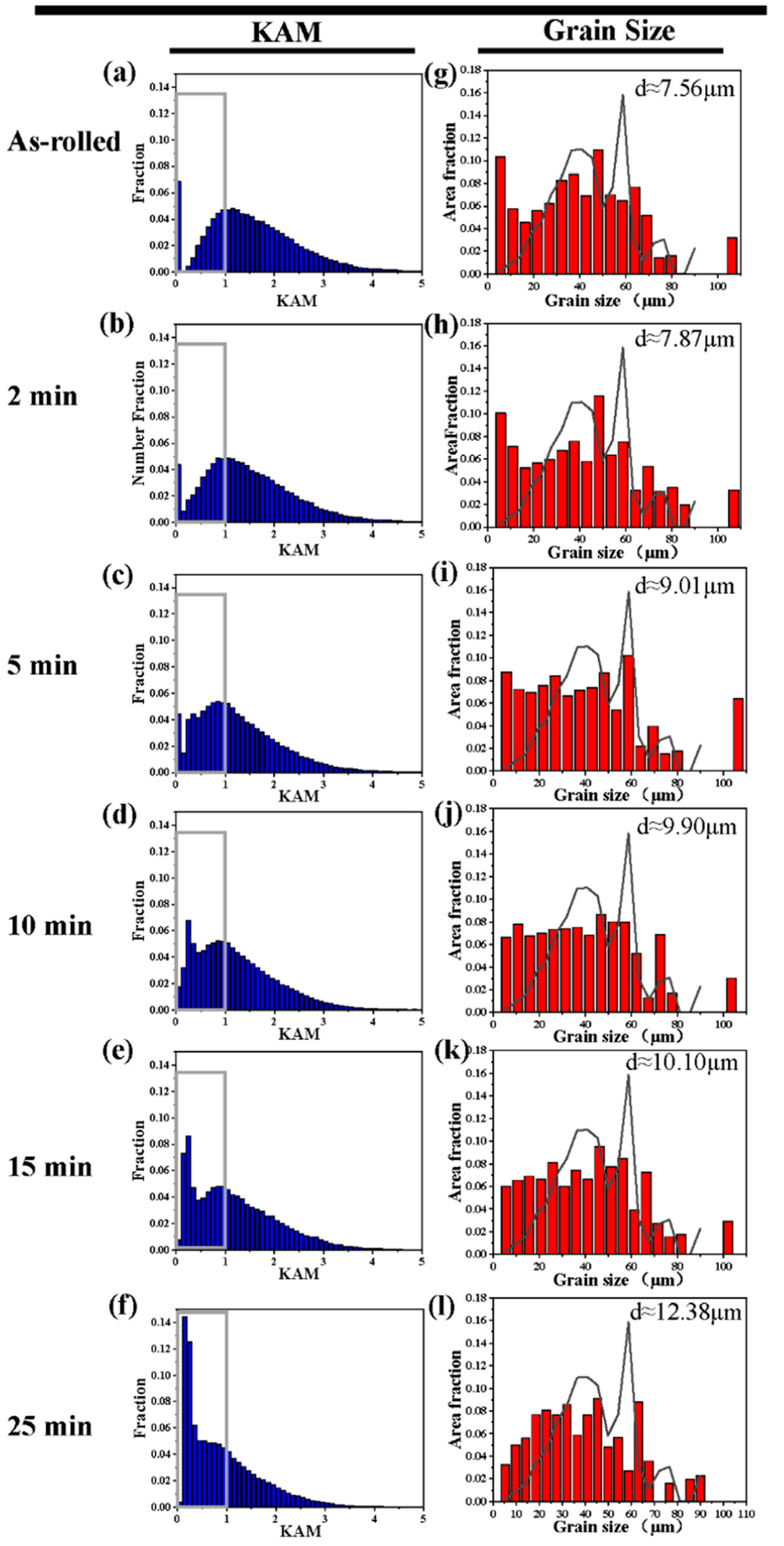

Fig. 5. (a-f) Kernel average misorientation (KAM) and (g-l) grain size distribution evolution of cold rolled sample during annealing: (a, g) cold rolled samples, (b, h) 2 min, (c, i) 5 min, (d, j) 10 min, (e, k) 15 min and (f, l) 25 min. The black lines in g-l are the grain size distribution of as-extruded sample.

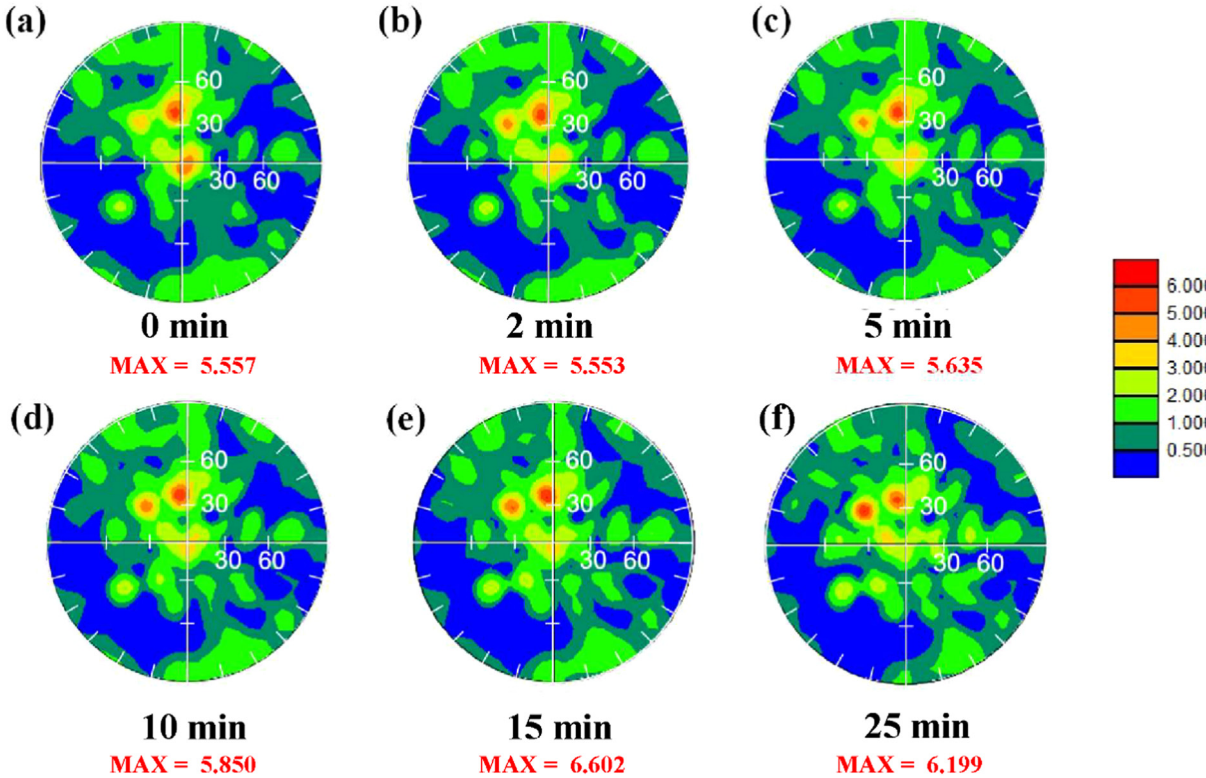

Fig. 6. (0001) pole figures evolution during annealing: (a) cold rolled, (b) 2 min, (c) 5 min, (d) 10 min, (e) 15 min and (f) 25 min.

as marked by the black circle, plenty of nucleation formed within {10–12} twins or nucleated at the impingements of {10–12} twin variant and {11–21} twin variants. In the black circle (Fig. 8b), three SRXed grains (marked as 1–3) grow up apparently during subsequent annealing, and other SRXed grains nucleated within black circle as well as partial {10–12} and {11–21} twin crystals were greatly consumed owing the growth of 1–3. SRXed grains (marked as 4 and 5) can be observed at the grain boundaries of G5 after 25 min annealing and consumed partial twins and parent grain (Fig. 8d). SRXed grains 1–5 show various orientation and made a great contribution on the consumption of basal oriented microstructure (Fig. 8d and h). Although the SRXed grain grew quickly, grains that formed within G5 (1–3) still confined by the boundaries of parent grains. Interestingly, different from the detwinned {11–21} twin variant in G4 (Fig. 7b), partial {11–21} twin variants keep stable and some of them even expanded and consumed the {10–12} twins after annealing for 25 min (marked by white arrows in Fig. 8d).

In Fig. 9, the grain (G6) that {11–21} twinning predominated in twinning behaviors was selected. Two {10–12} twin variants (T1-T2) and two {11–21} twin variants (T3-T4) activated, and the morphology of twin crystals are serrated in G6. As marked by black circles in the cold rolled state (Fig. 9a), many new grains and sub-grains formed at the twin boundaries or twin boundaries impingements [31]. During annealing, SRXed grains formed dispersedly and grew up quickly. Almost all parent grain and original twin crystals were rapidly consumed by the new formed grains and twin boundaries show barely confine to these SRXed grains. After 15 min annealing, 13 SRXed grains formed and their orientation are close to the original {10–12} and {11–21} twin crystals (T1-T4).

Fig. 10 shows the evolution of the twinned grains with irregular {10–11} twins. One basal oriented {10–12} twin variant (T1) and two non-basal oriented {11–21} twin variants (T2 & T3) can be seen (Fig. 10a). Further, two {10–11} twin variants activated (T11 & T12) within T1 and most parts of T11 exhibit irregular shape owing to twin-twin interaction [34], which can hardly operate in previous work. After 2 min annealing (Fig. 10b and f), despite the SRXed grains (2, 3, 6, 7, 9 and 10–12) that still remained after 25 min annealing, plenty of grains that show various orientations nucleated (marked by black arrows) and most of them nucleated at the intersection between {10–11} twin and other twin crystals. Obviously, the serrated boundaries are favorable for SRXed nucleation [35]. After 25 min annealing (Fig. 10d and h), there were 12 grains remained and most initial microstructure and SRXed grains were consumed by these 12 grains. Grains, i.e., 10, had expanded across the initial boundaries of the twinned grain. The black circles on the (0001) scattered pole figures exhibit the orientation distribution of initial microstructure where SRXed grains nucleated. The basal oriented {10–12} twin crystals almost exhausted while most large SRXed grains show the orientation near or within the circles after anneal-

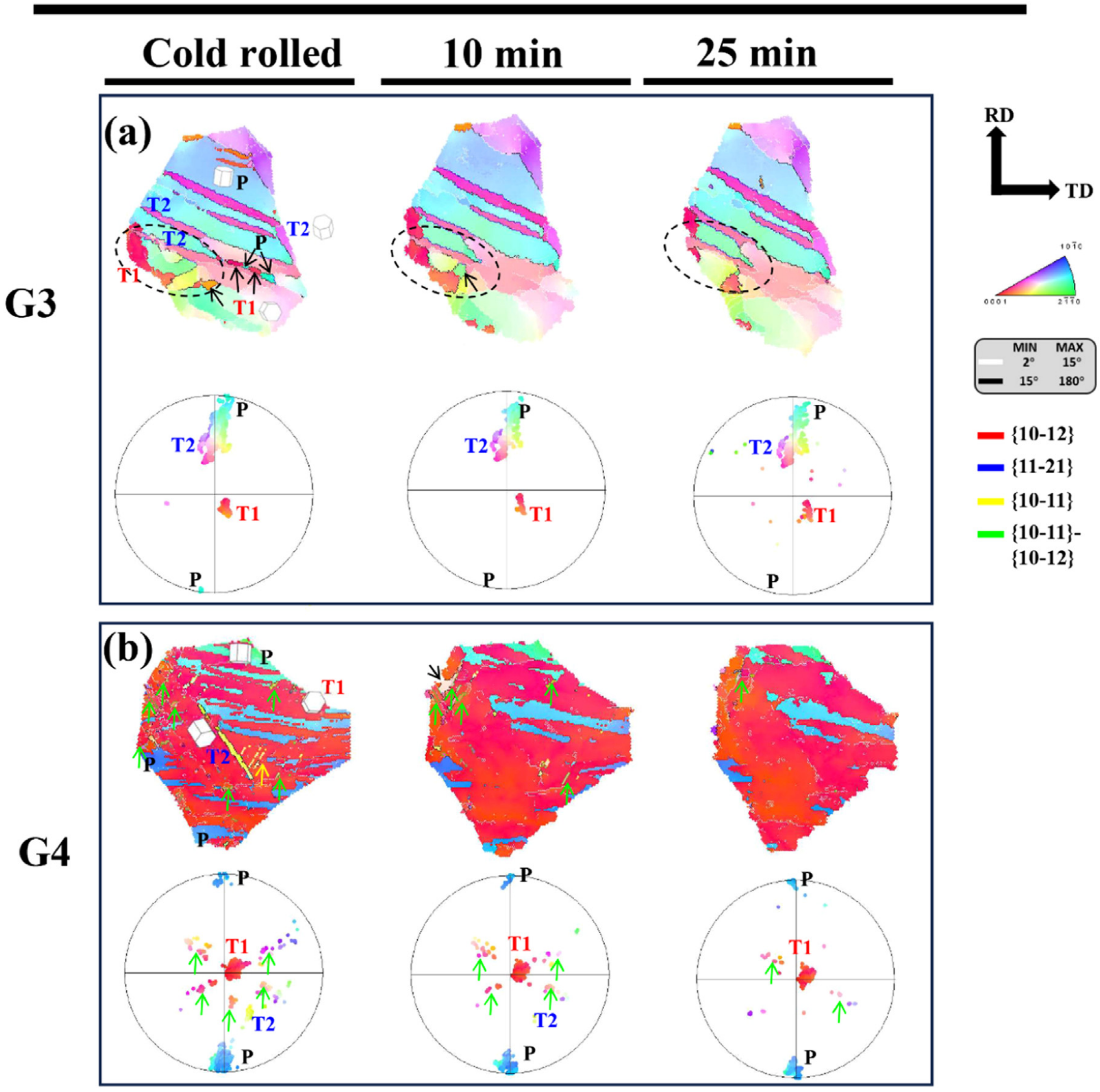

Fig. 7. Microstructure evolution and corresponding (0001) scattered pole figures of twinned grains with rare SRX: (a) G3 and (d) G4.

ing for 25 min (Fig. 10d and h), which is similar to that in G6 and indicate contribution of SRX on basal component weakening.

4. Discussion

4.1. Analysis on the twin induced SRX

Different from the traditional twin induced SRX mentioned in Section 1, SRX rarely occurred within lenticular compression {10–11} or {10–11}-{10–12} double twins and most of them detwinned or consumed by growing SRXed grains. For {10–12} twins, SRX occurred in some basal oriented {10–12} twin crystals (Fig. 8) while absent in the others (Fig. 7b). Similar to the SRX in {10–12} twins, the SRX operated optionally within {11–21} twins (Fig. 7-10). During annealing, it is widely accepted that the SRX usually prefer operating within twins with high storage energy [17,22,36]. The KAM map of twinned grains G3-G7 (cold rolled state) are shown in Fig. 11. In general, G3 show low KAM values in both parent grain and twins compared to other grains, which can be responsible for SRX absence. In G4-G7, we can see high storage energy areas within parent grains and twins (Fig. 11b-e) and obviously the high storage energy is beneficial to SRX. Interestingly, although we can sight high storage energy areas within {10–12} twins in G4 (Fig. 11b), SRX absent in this grain. This odd phenomenon become more prominent in the compression between G4 and G5 because their twinning behaviors and the orientation of microstructure resemble to each other closely, while SRX only operated within the {10–12} twins in G5 (Fig. 8). Hence, there must be other factors which functioned to the SRX.

As mentioned above, the types of dislocation play an important role on SRX in Mg alloys [24]. In addition, basal

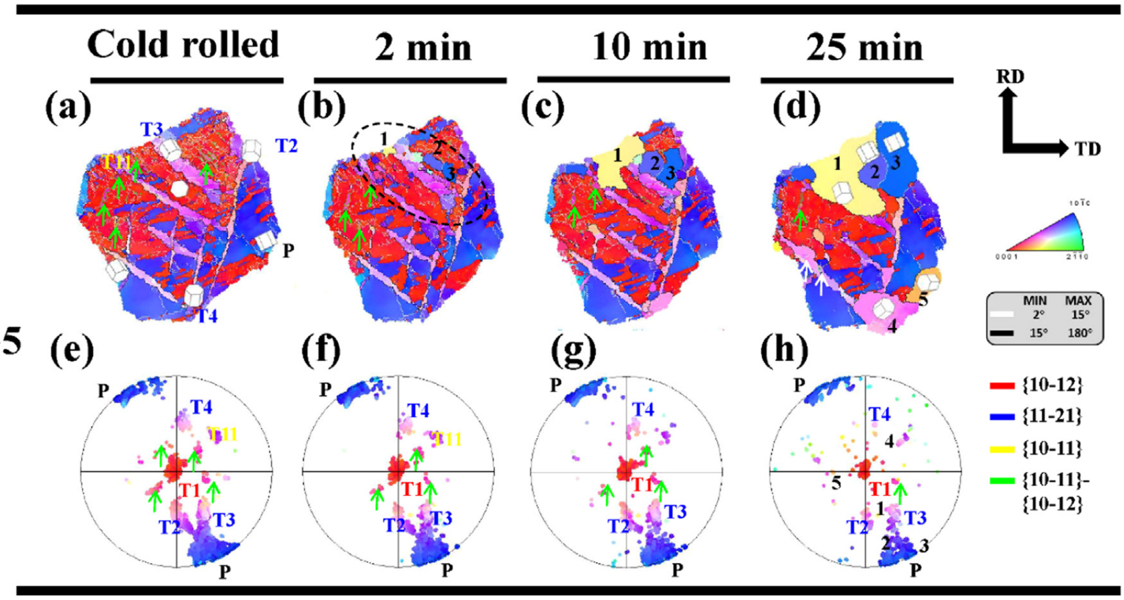

Fig. 8. SRX in the typical grain G5 that basal oriented {10–12} twin predominate in twins. (a-d) Inverse pole figure maps and (e-h) corresponding (0001) scattered pole figures evolution during annealing.

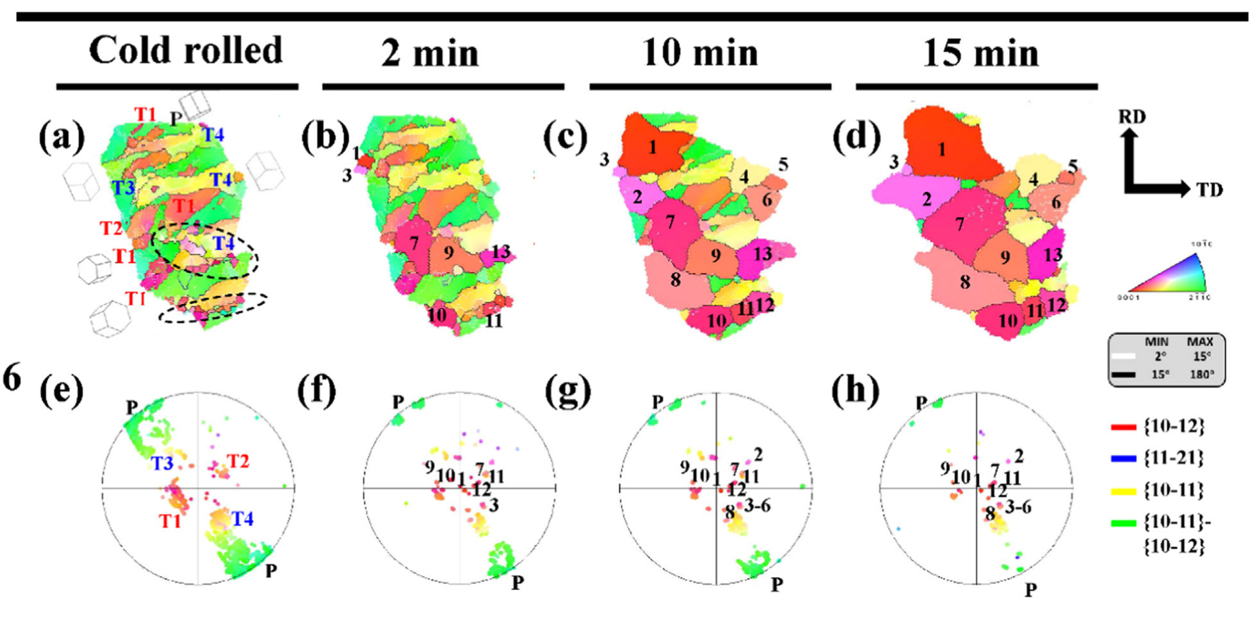

Fig. 9. SRX in the typical grain G6 that {11–21} twins predominate in twins. (a-d) Inverse pole figure maps and (e-h) corresponding (0001) scattered pole figures evolution during annealing.

slip is always considered to be the key role of twin induced SRX and SRX is usually regarded as the results of cross slip and climb of the high density of basal <*a*>/prismatic ⟨a⟩ dislocation, i.e., typical SRX in compression and double twins [14,36]. However, the formation of 3 dimensional recrystallization nuclei required <c + a> dislocation [37,38] and contribution of <c + a> dislocation to twin induced SRX has rarely been discussed in previous work. The pyramidal <c + a> slip can activate under high strain rate deformation [29] and the RE elements solute are proposed to be beneficial for the activating of <c + a> slips in Mg-RE alloys [39,40]. Obviously, in the wrought Mg-RE alloy with severe deformation and high RE content, the influence of <c + a> dislocation to SRX should not be ignored. Therefore, G4 and G5 were selected out to analyze the influence of dislocation type to SRX owing to their different SRX behaviors. Intra-

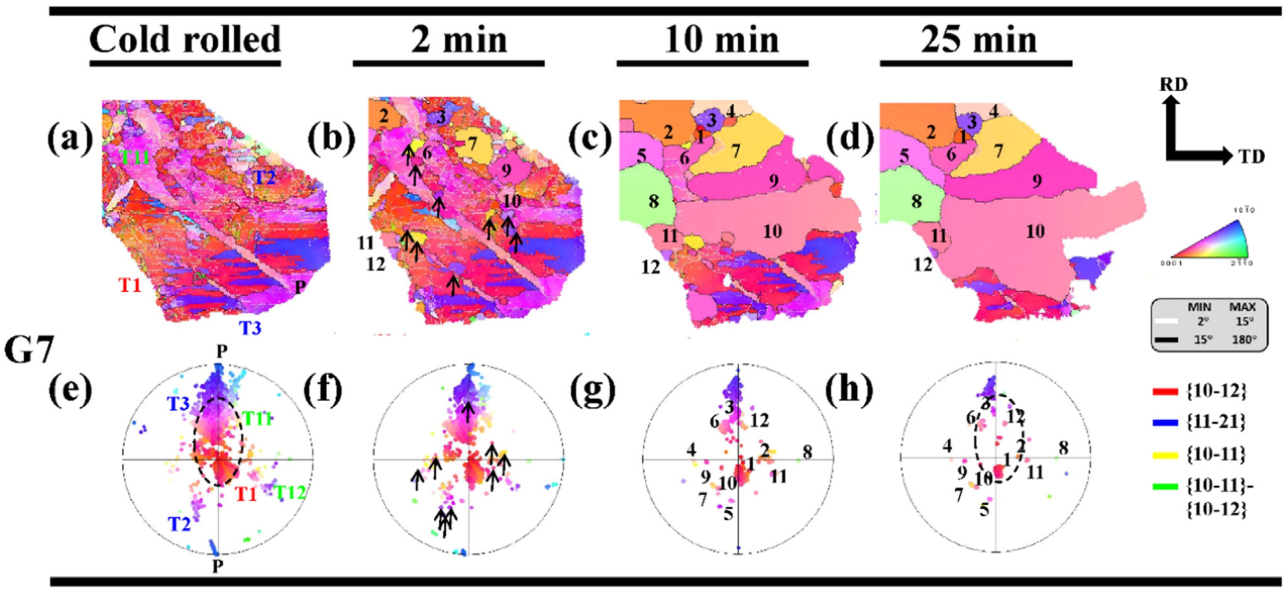

Fig. 10. SRX in the typical grain G7 that compression twins show irregular morphology owing to twin-twin interaction. (a-d) Inverse pole figure maps and (e-h) corresponding (0001) scattered pole figures evolution during annealing.

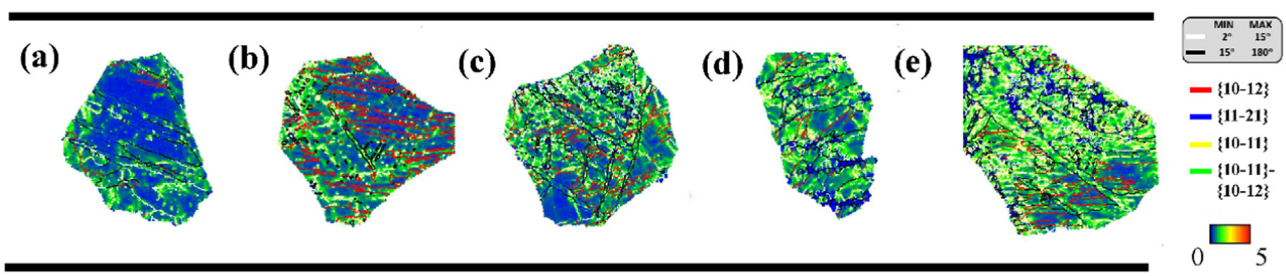

Fig. 11. KAM maps of selective grains G3-G7: (a) G3, (b) G4, (c) G5, (d) G6 and (e) G7.

granular misorientation axis (IGMA) analysis can be used to distinguish the dislocation types in Mg alloys [41,42] and the specific axes and related dislocations were summarized within Fig. 12 g [43,44]. As shown in Fig. 12c and f, although basal ⟨a⟩ dislocation and pyramidal-II <c + a> dislocation cannot be differentiated because of their common ⟨10–10⟩ axis, the pyramidal-I <c + a> dislocation can be identified according to IGMA results. Considering the low rolling temperature which is favorable for basal slip activating, it can be concluded that the <c + a> dislocation and basal <a> dislocation occurred in both G4 and G5 (Fig. 12c and f). Obviously, more condition should be considered to explain the difference between G4 and G5 in SRX.

As shown in scattered pole figures in Figs. 7-10, the parent grains and twins exhibit broad distribution, which indicate the huge orientation change within the twinned grains, and such misorientation distribution may cause discrepant dislocation distribution. It is proposed that the dislocation type can be reflected by the grain reference orientation deviation (GROD) axis [45] and GROD angle can reflect the dislocation density distribution [46]. Therefore, we depicted the GROD axis of selective grains (G4 and G5) and the GROD angle maps of {10–12} twins within selective grains to analyze the dislocation distribution condition. Grain average orientation was selected as reference orientation [46]. As shown in Fig. 12a, the {10–12} twin crystals outside the black circle can be divided into several major areas according to colors. Area with similar color share similar GROD axis, which indicate the activation of the same slip system. Therefore, it can be inferred that different dislocations clustered within different areas and the same dislocation clustering is disadvantageous for cross slip and dislocation interaction, which thus result in the fewer LAGBs outside the black circle although high dislocation density can be identified in these areas (Fig. 12b). In the black circle in Fig. 12a, mix of multiple colors indicated various dislocation activating and this can be proved by the high density of LAGBs (Fig. 12b). Although no visible SRXed grains can be observed finally after annealing, sub-grains can be observed within the double twins and grow through the constrain of double twin boundaries (marked by the black arrow in Fig. 7b). The absence of SRX within the black circle in Fig. 12a may mainly result from the numerous double twin

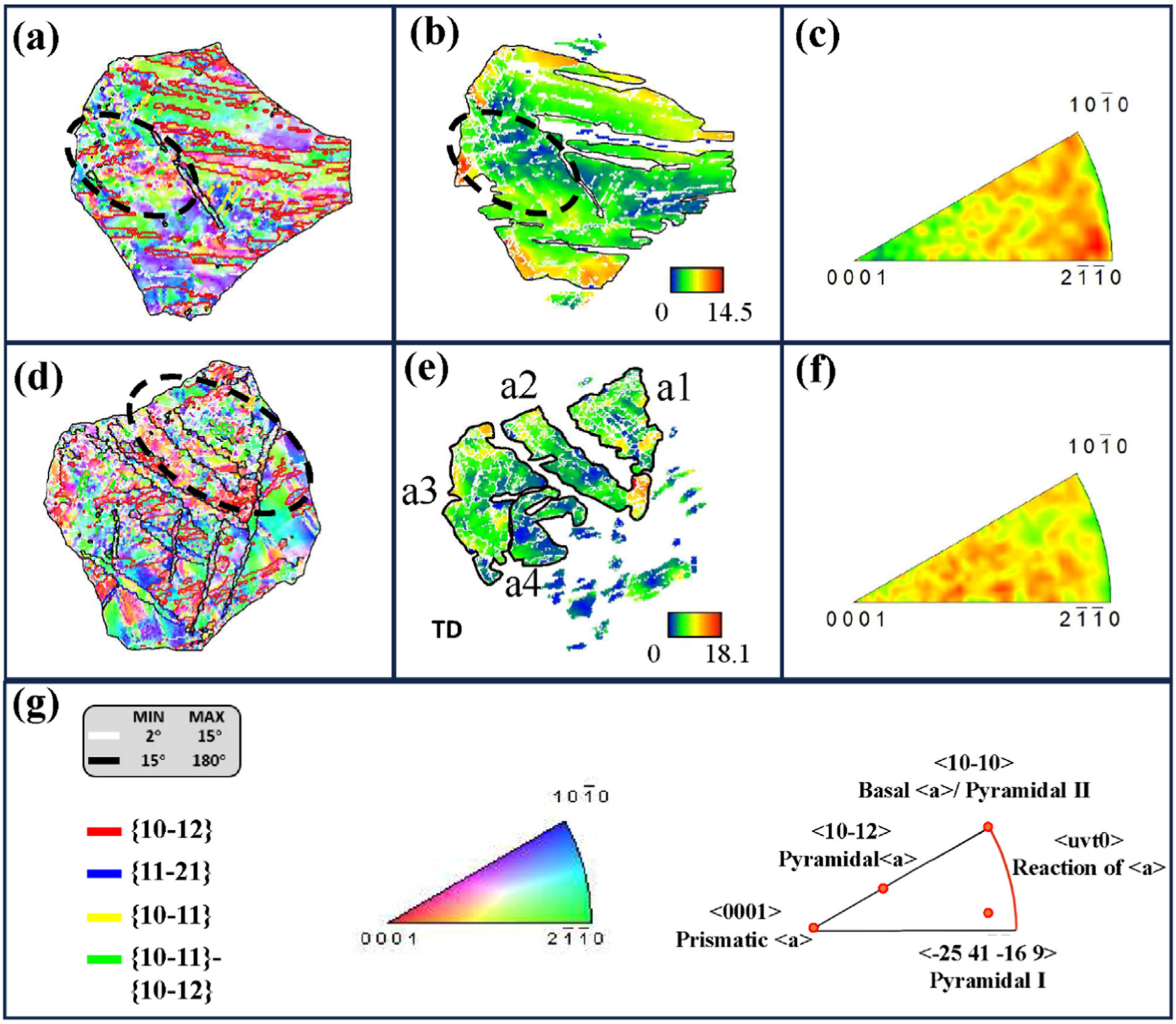

Fig. 12. EBSD results of (a-c) G4 and (d-f) G5: (a, d) grain reference orientation deviation-axis maps, (b, e) grain reference orientation deviation-angle maps of {10–12} twin crystals and (c, f) IGMA result of G4 and G5. (g) Specific rotation axes and related dislocation types [43,44].

which may interact with dislocation and detwinned during annealing (Fig. 7b) and the low dislocation density (Fig. 12b). Four main {10–12} twin crystals in Fig. 12d were extracted to further confirm the function of <c + a> dislocation to SRX and a large degree value was chosen for the IGMA intensity plot of these twin crystals to show the results clearly. As mentioned in Fig. 8a-d, SRX occurred within a1 and a2 but absent within a3 and a4, which can be attributed to the influence of dislocation distribution. In the twinned areas (a1 and a2), pyramidal-I <c + a> dislocation can be identified along with the basal <a>/ pyramidal-II <c + a> (Fig. 13e-f) and the mix of multiple color of the GROD axis map (Fig. 12d) reveal the interaction of these dislocations, which finally result in the SRX during annealing. In a3 and a4, the GORD axis map can also reveal the complex slip modes (Fig. 12d). However, the IGMA results (Fig. 13 g and h) indicate the low density of <c + a> dislocation, which will restrict the formation of 3-dimensional dislocation network and subsequent SRXed grain forming. The SRX in {11–21} twins, i.e., in G5 and G6, can also be explained as same approach. Therefore, it can be concluded that the activation of <c + a> dislocation and related dislocation interaction strengthened the SRX during annealing in this work.

In addition, SRX absent in most compression and double twins in this work, which is induced by the activation of <c + a> dislocation. As mentioned before, <c + a> dislocation in this work is active due to the high strain rate and Gd content [29,39,40]. As shown in Fig. S5, the IGMA results of selective area with abundant twinned grains indicate the various slip systems activating rather than the strengthened <a> dislocation. Owing to the activation of <c + a> dislocation, the components which are unfavorable for basal/prismatic slips activating can accommodate strain through the activation of <c + a> slips, which release the strain concentration within compression/double twins and thus responsible for the absence of SRX. The competition between <c + a> slips

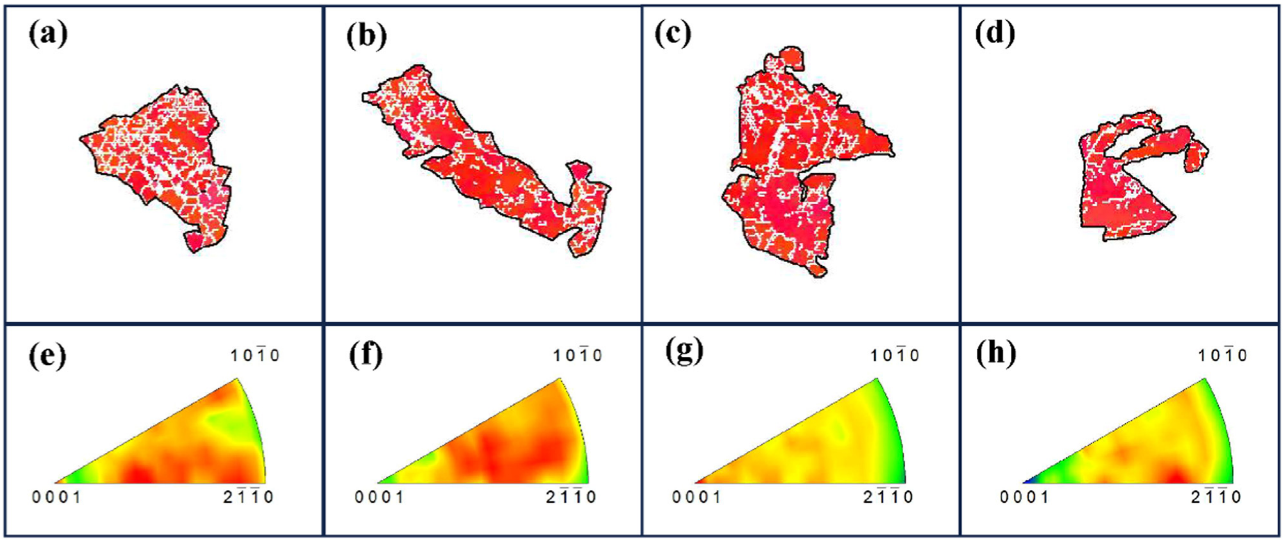

Fig. 13. (a-d) Inverse pole figure maps of {10–12} twin crystals a1-a4 in G5 and corresponding (e-h) IGMA results: (a, e) a1, (b, f) a2, (c, g) a3 and (d, h) a4.

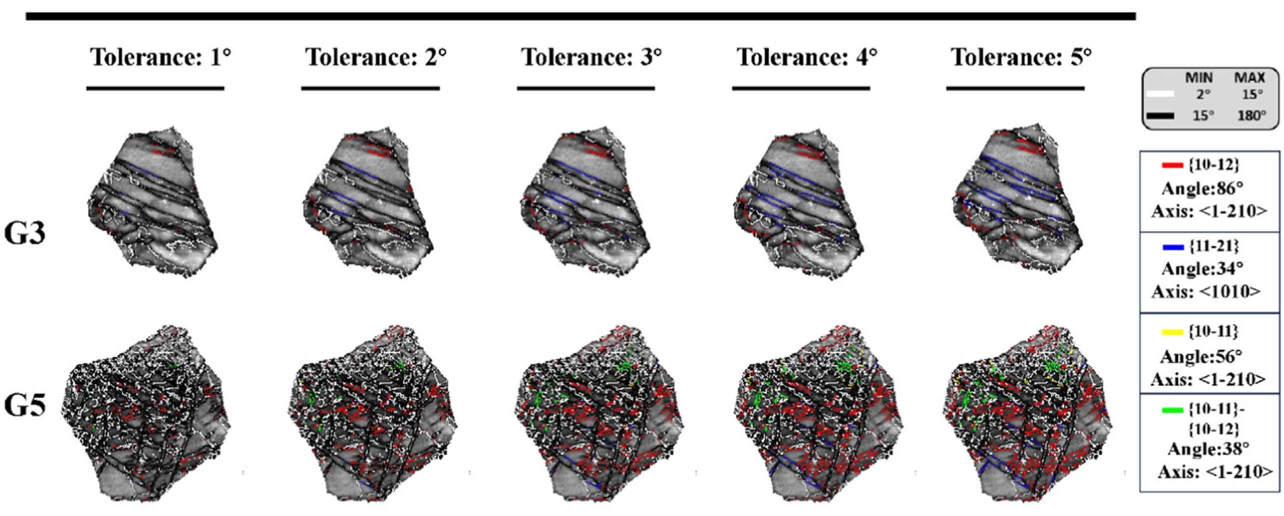

Fig. 14. Twin boundaries identification of G3 and G5 with various tolerance angles.

and compression/double twin can also explain the small size of most compression/double twins in the cold rolled samples (Figs. 7 and 8).

4.2. The thermal stability of various twin boundaries

As shown in G3-G7, most compression/double twins detwinned during annealing while extension twin, especially {11–21} twin, exhibit complicated thermal stability (Figs. 7-10). In addition, as shown in Fig. 14, plenty of twin boundaries were identified as HAGBs with the tolerance decreasing, which suggest that the coherence of partial twin boundaries were actually damaged during cold rolling owing to the dislocation-twin interaction and work as HAGBs [47,48]. Therefore, both the property of incoherent twin boundaries (HAGBs) and coherent twin boundaries should be considered for the migration of twin boundaries. For the coherent twin boundaries, twin boundaries will migrate or lose coherence when interact with different dislocations [47–50], i.e., the dislocation will be absorbed by twin boundaries when the Burgers vector of dislocation is not parallel to the zone axis of twin [50]. In addition, the solute segregation can also retard the migration of twin boundaries [51,52]. For HAGBs, the migration is mainly closely related to the storage energy, grain size difference, grain boundary property and solute segregation [25]. Therefore, the twin boundaries migration in this work were mainly discussed in the above aspects. For the convenience of discussion and description, the incoherent parts were regard as the HAGBs in this section.

Usually, storage energy can drive the migration of grain boundaries [53]. As displayed in Fig. 11a, {11–21} twin exhibit low storage energy and thus keep stable during annealing, while {11–21} twins in other grains (G4-G7) with high storage energy enlarged or shrunk in addition to SRX. Obviously, the high storage energy will drive the migration of incoherent twin boundaries. Further, the high storage energy always indicates the high dislocation density and various dislocations can be identified according to the IGMA and GORD results (Fig. S5, Figs. 12 and 13). It is proposed that interaction between twin boundaries and specific dislocations can result in facets and steps along twin boundaries, which can act as twinning dislocation source and thus promote the migration of twin boundaries [49]. Various dislocation can be identified in the cold rolled grains (Fig. 13), which can be responsible for partial coherent twin boundaries migration through the activation of twinning dislocation. In addition, twin boundaries may lose coherency when specific dislocations migrate and react with them [28,50], and migrate under the driving of storage energy during subsequent annealing. As marked by red arrows in Fig. S6, in the area with high storage energy, partial {10–12} twin boundaries transformed to HAGBs and moved constantly during annealing. On the contrary, the twin boundaries without suitable dislocation-twin interaction and storage energy driving can thus keep stable (Figs. 7-10).

As displayed in Figs. 7–10, most compression/double twins with small size detwinned, which can be attributed to the effect of grain size. The grain with large size will grow preferentially [54]. The high dislocation density within basal oriented {10–12} twins can cause the incoherent compression/double twin boundaries (Fig. 14), and the compression/double twins with small size thus vanished during annealing owing to the grain size effect. In Mg alloys, RE elements, i.e., Gd and Y, prefer segregating at twin boundaries [51,55,56]. Maghsoudi et al. proposed that the segregation of Gd can restrict the migration of {10–12} twin boundaries by pinning the twin boundaries [56]. Somekawa et al. found that the Y solute which segregate at twin boundaries can stabilized {10–12} twin boundaries during annealing [51]. For the twin boundaries (especially the coherent boundaries) that formed at room temperature, there are usually no solute segregation and the solute will gradually segregate at twin boundaries during annealing [57]. As shown in Fig. 15a-d, no obvious solute segregation can be identified before annealing according to the STEM-EDX results. Therefore, the migration of twin boundaries should be gradually slower with the annealing time increasing. As shown in Fig. 7 and 8, partial parent grains/twins which surrounded by {10–12} twin boundaries still vanished during annealing and these vanished areas always show small size or complex dislocation intersection (Fig. 12a and d), which indicate the combined action of dislocation interaction and grain size. In addition, no obvious migration retardation of twin boundaries can be observed, which indicate that solute segregation functioned little in this work. Considering our annealing temperature and time, the migration of twin boundaries should be mainly attributed to the common effects of storage energy, grain size and dislocation interaction.

Table 1
Misorientation angles and axes between SRXed grains and twins in G5 and G7.

SRXed grain	{10–11} twin	{10–12} twin
G5–1	/	62.63° [6 −14 8 5]
G5–2	/	85.73° [−13 −10 23 −2]
G5–3	/	85.42° [18 −7 −11 1]
G7–2	53.36° [−6 0 6 1]	24.49° [−1 −12 13 7]
G7–5	86.91° [−15 −16 1 −4]	42.01° [22 −13 9 1]
G7–7	60.84° [−5 7 −2 2]	40.67° [6 5 −11 3]
G7–8	83.91° [−13 −10 23 4]	54.54° [1 −29 28 2]
G7–9	45.79° [6 −3 −3 −2]	51.20° [0 11 −11 2]
G7–10	70.69° [12 −11 1 −2]	62.63° [13 5 −18 10]

4.3. Mechanism for the preferential grain growth

As displayed in Fig. S2, several main poles gradually strengthened during annealing, which indicate the preferential grain growth of the SRXed grains. The preferential grain growth can be seen in Figs. 8-10 and initial microstructure were greatly consumed by SRXed grains. As displayed in Figs. 8-11, it can be obviously concluded that the effects of grain size and storage energy functioned little to preferential grain growth owing to the large size of deformed microstructure and the uniformly distributed storage energy (Fig. 11). Owing to our short annealing time, the solute segregation and relate effect to grain boundary migration should be slight. Therefore, the effect of grain boundary property should be the main contributor. In Mg alloys, HAGBs with specific misorientation angle and rotation axis were called near-coincident site lattice (CSL) boundary [58]. It is proposed that near-CSL boundary greatly influence the grain boundary precipitates distribution and the grain boundary migration [25,59]. The misorientation angles and axes between SRXed grains and twins that were greatly consumed in G5 and G7 were summarized in Table 1. The SRXed grains with large size were considered. As displayed in Table 1, some of these fast-moving grain boundaries approach to several specific near-CSL boundaries, i.e., Σ13b (85.59°, [10–10]), Σ17a (86.63°, [2-1-10]), Σ17b (49°, [10–10]) and Σ21 (70°, [70–72]) [58], which may indicate the high mobility of these near-CSL boundary in this work.

As shown in Fig. 6 and S2, the texture of all microstructure and SRXed grains are close to stable state after annealing for 15 min, which indicate that the fast growth of SRXed grains approach the end. The misorientation distribution curves after annealing for 15 min and 25 min exhibit similar shape, which indicate that the grain boundaries between identified grains were stable after annealing for 15 min (Fig. 16). In addition, as marked by the black arrows in Fig. 16, the grain boundaries with marked misorientation angles decreased anomalously after annealing for 15 min, which suggest that these grain boundaries are unstable. To identify the property of these boundaries, axis and angle distribution of SRXed

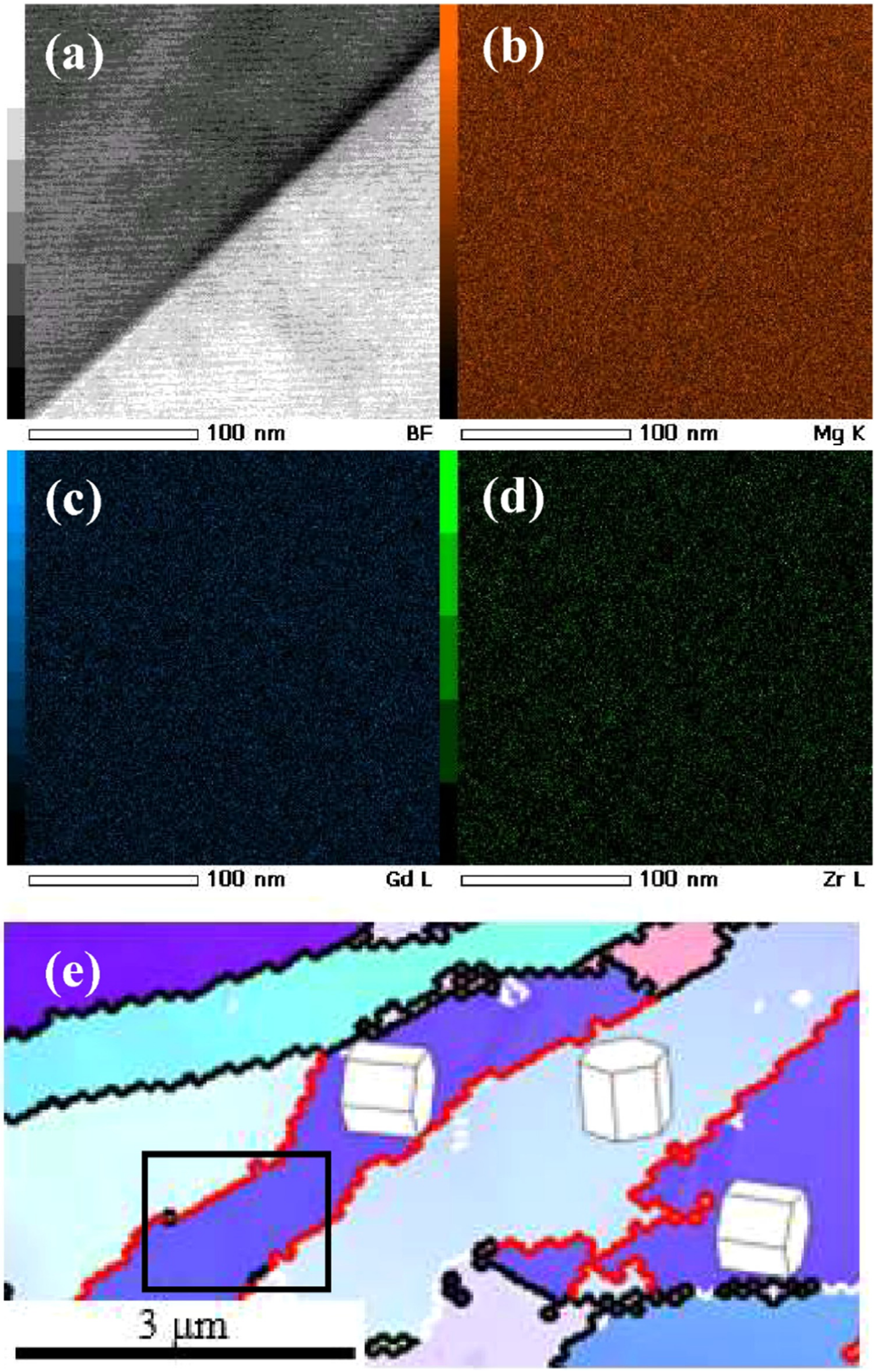

Fig. 15. (a-d) STEM-EDX results of {10–12} twin boundaries: (a) STEM image, (b-d) STEM-EDX map results of Mg, Gd and Zr. (e) EBSD inverse pole figure map of the TEM sample. The twin boundaries in a-d were marked by black rectangular in e and identified as {10–12} twin boundaries.

grains after annealing for 2 min and 15 min were summarized in Fig. 17. As shown in Fig. 17, grain boundary length decreased with the annealing time increasing at 0–20° and favorable axis [0001] can be observed (Fig. 17k), which reveal the stability of grain boundaries with 10–20° and [0001] axis. At the misorientation range of 20–50°, the grain boundary number increased while the favorable axes [10–10] for 30–40° and 40–50° become weakened, which indicate the high mobility of the boundaries with 30–50° and [10–10] axis. At 50–70°, the stable grain boundaries with [10–10] axis and 50–70° as well as with axis [2–1–10] and 60–70° can be identified. At 70–90°, the grain boundary number increased firstly

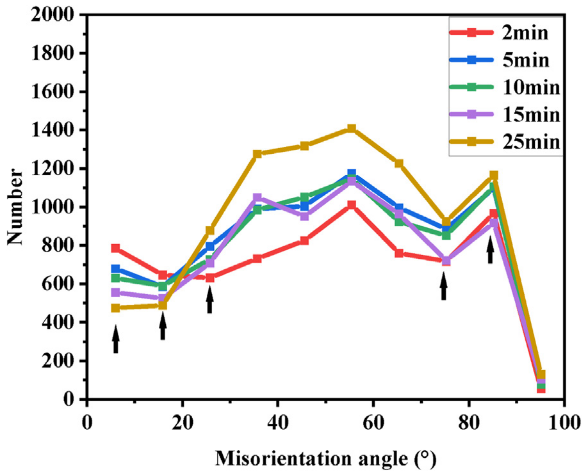

Fig. 16. Misorientation angle distribution evolution of SRXed grains. Only grain boundaries between identified grains were counted.

Table 2
The possible near-CSL boundaries which approach to the specific SRXed grain boundaries with high mobility [58].

Σ	10	14	15b	**17a**	**17b**	**21**	23c	23d
Angle/°	78.46	44.42	86.18	86.63	49.68	73.40	77.44	34.30
Axis/[]	10–10	10–10	2–1-10	2–1-10	10–10	70–72	2–1-10	10–10
c/a	1.633	1.633	1.620	1.633	1.620	1.620	1.620	1.620

(2min-10 min) and then decreased (15 min) obviously, which indicate that the grain boundaries with specific rotation axes ([10-10] and [2-1-10]) are unstable (Figs. 16 and 17). The near-CSL boundaries that approach abovementioned specific boundaries with high mobility were summarized in Table 2. Σ17a, Σ17b and Σ21 can also be identified in Table 2, which is corresponding to the grain boundaries with high mobility in the twinned grains (Table 1). Therefore, it can be concluded that these specific near-CSL boundaries may have high mobility and thus cause the preferential grain growth in this work.

5. Conclusions

In summary, quasi-in-situ observation was carried out on the cold rolled high Gd content Mg alloys with {11–21} twins to analyze the evolution of microstructure and texture and basal component weakening is achieved. The main conclusions are summarized as follows:

1. The basal component was gradually weakened owing to the consumption of basal oriented {10–12} twins. SRX can be widely observed within {10–12} and {11–21} twins but absent in most double twins and compression twins, which is different to traditional twin induced SRX in Mg alloys.
2. During annealing, the SRXed grains exhibited preferential grain growth. Despite the twins consumed by SRXed grains, most small-sized compression/double twins detwinned while only partial {11–21} and {10–12} twins detwinned.
3. The serrated twin boundaries induced by the interaction between {11–21} twin and other twins can act as nucleation sites and thus promote the SRX. <c + a> dislocation and related dislocation interaction promote the operation of SRX in {10–12} and {11–21} twins by promoting the formation of new HAGBs during annealing. Activation of profuse <c + a> dislocation in the basal oriented microstructure accommodate the strain and thus release the strain concentration within compression/double twins, which is responsible for the SRX absence in most compression/double twins.
4. The migration of twin boundaries and related detwinning were mainly result from the small sizes of twins, storage energy difference and dislocation-twin interaction. High mobility of specific near-CSL boundaries mainly cause the preferential grain growth of SRXed grains.

Declaration of competing interest

The authors declare that they have no known competing financial interests or personal relationships that could have appeared to influence the work reported in this paper.

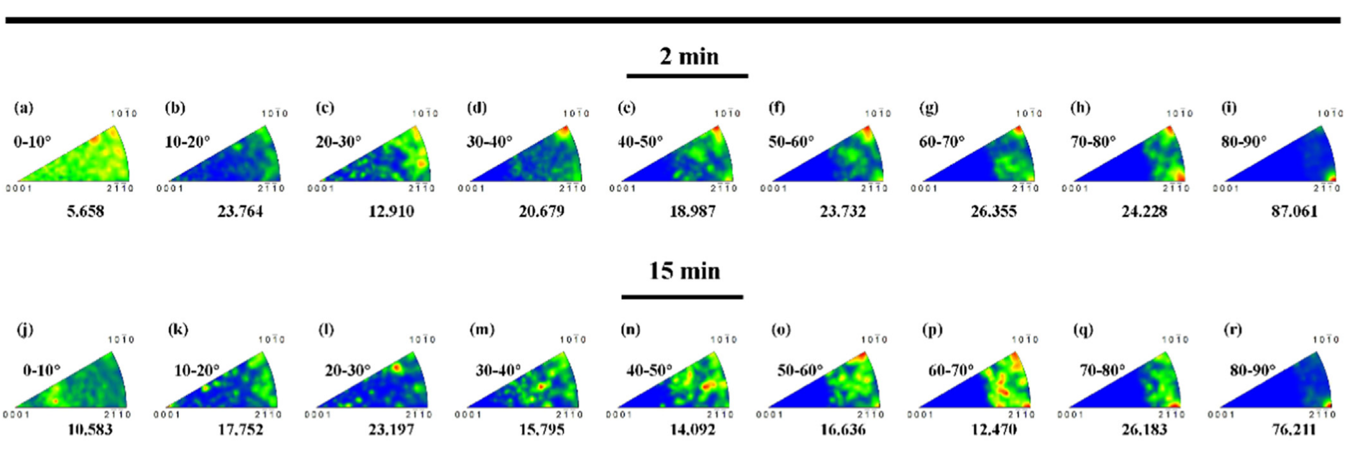

Fig. 17. Axis and angle distribution after annealing for (a-i) 2 min and (j-r) 15 min.

CRediT authorship contribution statement

Ning Lv: Writing – review & editing, Writing – original draft, Software, Methodology, Conceptualization. **Lingyu Zhao:** Writing – review & editing, Validation, Supervision, Formal analysis. **Hong Yan:** Writing – review & editing, Supervision, Funding acquisition. **Boyu Liu:** Data curation, Supervision. **Rongshi Chen:** Funding acquisition, Resources, Supervision. **Zhiwei Shan:** Data curation, Supervision.

Acknowledgement

This work was financially supported by the National Natural Science Foundation of China (Nos. 52301164, 52371121 and 52271107).

Supplementary materials

Supplementary material associated with this article can be found, in the online version, at doi:10.1016/j.jma.2024.04.015.

References

[1] K. Zhang, Z. Shao, J. Robson, Y. Huang, J. Zheng, J. Jiang, J. Mag. Alloy. 11 (9) (2023) 3130–3140, doi:10.1016/j.jma.2023.09.002.
[2] S. Liu, H. Liu, X. Chen, G. Huang, Q. Zou, A. Tang, B. Jiang, Y. Zhu, F. Pan, J. Mater. Sci. Technol. 113 (2022) 271–286, doi:10.1016/j.jmst.2021.09.065.
[3] L. Liu, J. Li, S. Bai, B. Jiang, C. He, J. Zhou, G. Huang, D. Zhang, F. Pan, J. Mater. Sci. Technol. 178 (2024) 143–154, doi:10.1016/j.jmst.2023.08.036.
[4] B. Zhang, Y. Wang, L. Geng, C. Lu, Mater. Sci. Eng. A. 539 (2012) 56–60, doi:10.1016/j.msea.2012.01.030.
[5] H. Yan, X.H. Shao, H.P. Li, R.S. Chen, H.Z. Cui, E.-H. Han, Scr. Mater. 207 (2022) 10.1016/j.scriptamat.2021.114257.
[6] Z.R. Zeng, Y.M. Zhu, S.W. Xu, M.Z. Bian, C.H.J. Davies, N. Birbilis, J.F. Nie, Acta Mater. 105 (2016) 479–494, doi:10.1016/j.actamat.2015.12.045.
[7] H. Wang, D.T. Zhang, C. Qiu, W.W. Zhang, D.L. Chen, J. Mater. Sci. Technol. 163 (2023) 32–44, doi:10.1016/j.jmst.2023.03.057.
[8] Z.R. Zeng, M.Z. Bian, S.W. Xu, C.H.J. Davies, N. Birbilis, J.F. Nie, Scr. Mater. 108 (2015) 6–10, doi:10.1016/j.scriptamat.2015.06.009.
[9] J.H. Lee, S.H. Park, S.-G. Hong, J.W. Won, C.S. Lee, Scr. Mater. 99 (2015) 21–24, doi:10.1016/j.scriptamat.2014.11.017.
[10] B. Song, Q. Yang, T. Zhou, L. Chai, N. Guo, T. Liu, S. Guo, R. Xin, J. Mater. Sci. Technol. 35 (10) (2019) 2269–2282, doi:10.1016/j.jmst.2019.03.045.
[11] J. Luo, H. Yan, L.W. Lu, R.S. Chen, A.R. Wu, F.C. Yin, J. Alloy. Compd. 883 (2021) 10.1016/j.jallcom.2021.160813.
[12] M.G. Jiang, H. Yan, R.S. Chen, J. Alloy. Compd. 650 (2015) 399–409, doi:10.1016/j.jallcom.2015.07.281.
[13] S.H. Lu, D. Wu, R.S. Chen, E.-H. Han, Mater. Des. 191 (2020), doi:10.1016/j.matdes.2020.108600.
[14] D. Guan, W.M. Rainforth, L. Ma, B. Wynne, J. Gao, Acta Mater. 126 (2017) 132–144, doi:10.1016/j.actamat.2016.12.058.
[15] J.H. Lee, J.U. Lee, S.-H. Kim, S.W. Song, C.S. Lee, S.H. Park, J. Mater. Sci. Technol. 34 (10) (2018) 1747–1755, doi:10.1016/j.jmst.2018.03.002.
[16] S.W. Lee, G. Han, T.-S. Jun, S.H. Park, J. Mater. Sci. Technol. 66 (2021) 139–149, doi:10.1016/j.jmst.2020.04.074.
[17] T. Nakata, C. Xu, L. Geng, S. Kamado, J. Mag. Alloy. 11 (9) (2023) 3200–3213, doi:10.1016/j.jma.2023.09.007.
[18] X. Li, P. Yang, L.N. Wang, L. Meng, F. Cui, Mater. Sci. Eng. A. 517 (1–2) (2009) 160–169, doi:10.1016/j.msea.2009.03.045.
[19] Y. Liu, Y. Li, H. Zhang, Q. Zhu, X. Qi, J. Wang, J. Wang, P. Jin, X. Zeng, Mater. Charact. 162 (2020), doi:10.1016/j.matchar.2020.110192.
[20] T. Nakata, C. Xu, L. Geng, S. Kamado, J. Alloy. Compd. 928 (2022), doi:10.1016/j.jallcom.2022.167154.
[21] S.W. Lee, S.H. Park, J. Alloy. Compd. 844 (2020), doi:10.1016/j.jallcom.2020.156185.
[22] S.H. Lu, D. Wu, R.S. Chen, E.-h. Han, J. Mater. Sci. Technol. 59 (2020) 44–60, doi:10.1016/j.jmst.2020.04.040.
[23] L.Y. Zhao, H. Yan, R.S. Chen, E.-H. Han, J. Mater. Sci. Technol. 60 (2021) 162–167, doi:10.1016/j.jmst.2020.05.027.
[24] L.Y. Zhao, H. Yan, R.S. Chen, E.-H. Han, Scr. Mater. 188 (2020) 200–205, doi:10.1016/j.scriptamat.2020.07.037.
[25] L.Y. Zhao, H. Yan, R.S. Chen, E.-H. Han, J. Mag. Alloy. 9 (3) (2021) 818–828, doi:10.1016/j.jma.2020.02.026.
[26] N. Stanford, R.K.W. Marceau, M.R. Barnett, Acta Mater. 82 (2015) 447–456, doi:10.1016/j.actamat.2014.09.022.
[27] M. Jahedi, B.A. McWilliams, P. Moy, M. Knezevic, Acta Mater. 131 (2017) 221–232, doi:10.1016/j.actamat.2017.03.075.
[28] H. Zhang, Y. Li, Y. Liu, Q. Zhu, X. Qi, G. Zhu, J. Wang, P. Jin, X. Zeng, J. Mater. Sci. Technol. 81 (2021) 212–218, doi:10.1016/j.jmst.2020.11.062.
[29] J.L. Li, D. Wu, R.S. Chen, E.H. Han, Acta Mater. 159 (2018) 31–45, doi:10.1016/j.actamat.2018.08.013.
[30] J. Li, Z. Dong, X. Yi, D. Wu, R. Chen, J. Mag. Alloy. 11 (7) (2023) 2285–2298, doi:10.1016/j.jma.2021.09.023.
[31] N. Lv, L. Zhao, H. Yan, B. Liu, Y. Mao, Z. Shan, R. Chen, J. Alloy. Compd. 966 (2023) 10.1016/j.jallcom.2023.171590.
[32] G.M. Lee, S.H. Park, J. Mag. Alloy. 11 (6) (2023) 2165–2181, doi:10.1016/j.jma.2022.09.008.
[33] X. Wang, Y. Yu, W. Chen, X. Zhang, D. Fang, W. Zhang, W. Wang, Mater. Sci. Eng. A. 859 (2022), doi:10.1016/j.msea.2022.144193.
[34] H. Chen, T. Liu, S. Xiang, Y. Liang, J. Alloy. Compd. 690 (2017) 376–380, doi:10.1016/j.jallcom.2016.08.154.
[35] X. Yang, Y. Okabe, H. Miura, T. Sakai, Mater. Des. 36 (2012) 626–632, doi:10.1016/j.matdes.2011.12.001.
[36] I. Basu, T. Al-Samman, Acta Mater. 96 (2015) 111–132, doi:10.1016/j.actamat.2015.05.044.
[37] A. Galiyev, R. Kaibyshev, G. Gottstein, Acta Mater. 49 (2001) 1199–1207, doi:10.1016/S1359-6454(01)00020-9.
[38] Z. Wu, R. Ahmad, B. Yin, S. Sandlöbes, W.A. Curtin, Science 359 (2018) 447–452, doi:10.1126/science.aap8716.
[39] S. Sandlöbes, M. Friák, S. Zaefferer, A. Dick, S. Yi, D. Letzig, Z. Pei, L.F. Zhu, J. Neugebauer, D. Raabe, Acta Mater. 60 (6–7) (2012) 3011–3021, doi:10.1016/j.actamat.2012.02.006.
[40] R. Ahmad, Z. Wu, W.A. Curtin, Acta Mater. 183 (2020) 228–241, doi:10.1016/j.actamat.2019.10.053.
[41] L. Li, C. Zhang, H. Lv, C. Liu, Z. Wen, J. Jiang, J. Mag. Alloy. 10 (1) (2022) 249–265, doi:10.1016/j.jma.2021.05.001.
[42] T. Li, J. Rao, J. Zheng, D. Yin, H. Shou, Y. Zhang, R. Shi, W. Jing, L. Xia, J. Mag. Alloy. 10 (6) (2022) 1581–1597, doi:10.1016/j.jma.2022.05.010.
[43] M. Yamasaki, K. Hagihara, S.-i. Inoue, J.P. Hadorn, Y. Kawamura, Acta Mater. 61 (6) (2013) 2065–2076, doi:10.1016/j.actamat.2012.12.026.
[44] T. Matsumoto, M. Yamasaki, K. Hagihara, Y. Kawamura, Acta Mater. 151 (2018) 112–124, doi:10.1016/j.actamat.2018.03.034.
[45] V. Tong, H. Jones, K. Mingard, Int. J. Refract. Metals Hard Mater. 103 (2022), doi:10.1016/j.ijrmhm.2021.105734.
[46] Y. Chen, L. Jin, J. Dong, F. Wang, Y. Li, Y. Li, H. Pan, X. Nie, Mater. Charact. 134 (2017) 253–259, doi:10.1016/j.matchar.2017.10.028.
[47] J. Zhang, G. Xi, X. Wan, C. Fang, Acta Mater. 133 (2017) 208–216, doi:10.1016/j.actamat.2017.05.034.
[48] H. El Kadiri, C.D. Barrett, J. Wang, C.N. Tomé, Acta Mater. 85 (2015) 354–361, doi:10.1016/j.actamat.2014.11.033.
[49] H. Su, X. Zhou, S. Zheng, H. Ye, Z. Yang, J. Mater. Sci. Technol. 66 (2021) 28–35, doi:10.1016/j.jmst.2020.06.017.

[50] P. Chen, F. Wang, B. Li, Acta Mater. 164 (2019) 440–453, doi:10.1016/j.actamat.2018.10.064.

[51] H. Somekawa, H. Watanabe, D.A. Basha, A. Singh, T. Inoue, Scr. Mater. 129 (2017) 35–38, doi:10.1016/j.scriptamat.2016.10.019.

[52] X.F. Chen, L.R. Xiao, Z.G. Ding, W. Liu, Y.T. Zhu, X.L. Wu, Scr. Mater. 178 (2020) 193–197, doi:10.1016/j.scriptamat.2019.11.025.

[53] M.G. Jiang, C. Xu, H. Yan, T. Nakata, Z.W. Chen, C.S. Lao, R.S. Chen, S. Kamado, E.H. Han, J. Mag. Alloy. 9 (5) (2021) 1797–1805, doi:10.1016/j.jma.2020.09.001.

[54] M.A. Steiner, J.J. Bhattacharyya, S.R. Agnew, Acta Mater. 95 (2015) 443–455, doi:10.1016/j.actamat.2015.04.043.

[55] H. Zhou, G.M. Cheng, X.L. Ma, W.Z. Xu, S.N. Mathaudhu, Q.D. Wang, Y.T. Zhu, Acta Mater. 95 (2015) 20–29, doi:10.1016/j.actamat.2015.05.020.

[56] M. Maghsoudi, H. Ovri, T. Krekeler, M. Ziehmer, E.T. Lilleodden, Acta Mater. 258 (2023), doi:10.1016/j.actamat.2023.119202.

[57] J.F. Nie, Y.M. Zhu, J.Z. Liu, X.Y. Fang, Science 340 (6135) (2013) 957–960, doi:10.1126/science.1229369.

[58] A. Ostapovets, P. Šedá, A. Jäger, P. Lejček, Scr. Mater. 64 (5) (2011) 470–473, doi:10.1016/j.scriptamat.2010.11.011.

[59] Z. Wang, H. Xiao, W. Chen, Y. Li, J. Geng, K. Li, P. Xia, M. Wang, X. Li, D. Chen, H. Wang, Mater. Charact. 197 (2023) 10.1016/j.matchar.2023.112703.